Rapid microwave sintering of centimetric zirconia: Scalability and electromagnetic-thermal-fluid-dynamic simulation

Charles Manière, Christelle Harnois, Guillaume Riquet, Thomas Grippi, Stéphanie Behar-Lafenetre, Sylvain Marinel

▶ **To cite this version:**

Charles Manière, Christelle Harnois, Guillaume Riquet, Thomas Grippi, Stéphanie Behar-Lafenetre, et al.. Rapid microwave sintering of centimetric zirconia: Scalability and electromagnetic-thermal-fluid-dynamic simulation. Journal of the American Ceramic Society, 2022, 106 (2), pp.848-859. 10.1111/jace.18787 . hal-03795354

HAL Id: hal-03795354

https://normandie-univ.hal.science/hal-03795354

Submitted on 4 Oct 2022

HAL is a multi-disciplinary open access archive for the deposit and dissemination of scientific research documents, whether they are published or not. The documents may come from teaching and research institutions in France or abroad, or from public or private research centers.

L'archive ouverte pluridisciplinaire **HAL**, est destinée au dépôt et à la diffusion de documents scientifiques de niveau recherche, publiés ou non, émanant des établissements d'enseignement et de recherche français ou étrangers, des laboratoires publics ou privés.

Rapid microwave sintering of centimetric zirconia: scalability and electromagnetic-thermal-fluid-dynamic simulation

Charles Manière[1]*, Christelle Harnois[1], Guillaume Riquet[1], Thomas Grippi[1,2], Stéphanie Behar-Lafenetre[2], Sylvain Marinel[1]

1. Normandie Univ, ENSICAEN, UNICAEN, CNRS, CRISMAT, 14000, Caen, France
2. Thales Alenia Space, 5 Allée des Gabians, 06150 Cannes, France

Keywords
Flash sintering; zirconia; microwave sintering; sintering mechanisms; simulation

Abstract

Microwave sintering is a method presenting the following advantages for flash sintering: contactless/volumetric heating, the possibility to control the heating cycle by the microwave power. In this study, the transition from typical 100 K/min to ultra-rapid heating rate 500 K/min is studied. The heating homogeneity of the typical hybrid configuration using silicon carbide susceptors is tested up to the stability limit of the system. We show that zirconia specimen as thick as 10 mm can be heated and sintered up to 500 K/min heating rate at which thermal cracks appear. However, the centimetric size of the specimens seems to favor coarsening implying an important remaining porosity in the end. A comprehensive simulation including the microwave heating and convection has allowed the determination of the heating regime transition during the flash process and the quantification of each specimen cooling fluxes.

Graphical Abstract

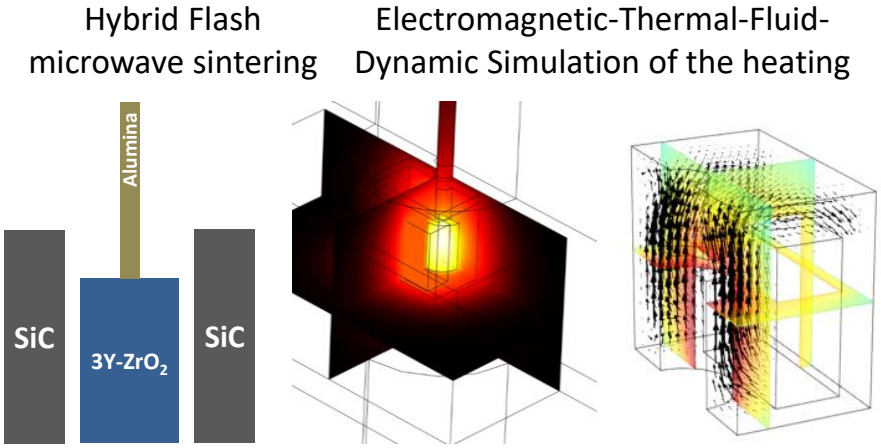

* Corresponding author: **CM**: Laboratoire de cristallographie et sciences des matériaux (CRISMAT), 6 Bvd du maréchal Juin 14050 CAEN CEDEX 4, France
Ph.: +33.2.31.45.13.69 ; *E-mail address*: charles.maniere@ensicaen.fr

Highlights

- Ultra-rapid microwave sintering of zirconia
- Electromagnetic-thermal-fluid-dynamic simulation of the heating
- Sintering kinetics analysis

Nomenclature

C_p Heat capacity ($J \cdot kg^{-1} \cdot K^{-1}$)
T Temperature (K)
κ Thermal conductivity ($W \cdot m^{-1} \cdot K^{-1}$)
Q_e Heat source ($W \cdot m^{-3}$)
φ_{rsa} Surface to ambient radiative heat flux ($W \cdot m^{-2}$)
σ_s Stefan Boltzmann constant ($5.67. \times 10^{-8}$ $W \cdot m^{-2} K^{-4}$)
ϵ Emissivity
T_{air} Air temperature (K)
φ_{csa} Convective heat flux ($W \cdot m^{-2}$)
h_{ia} Surface conductivity ($W \cdot m^{-2} \cdot K^{-1}$)
J Surface radiosity ($W \cdot m^{-2}$)
G Irradiation flux ($W \cdot m^{-2}$)
n Refractive index
$e_b(T)$ Surface radiation produced ($W \cdot m^{-2}$)
ρ_r Reflectivity
φ_{rss} Net inward radiative heat flux ($W \cdot m^{-2}$)
μ_r Complex relative permeability
ε_r Complex relative permittivity
μ_r'' Relative permeability imaginary part
ε_r'' Relative permittivity imaginary part
k_0 Vacuum wave number ($rad \cdot m^{-1}$)
σ Electric conductivity ($S \cdot m^{-1}$)
ε_0 Vacuum permittivity ($8.854187817. \times 10^{-12}$ $F \cdot m^{-1}$)
μ_0 Vacuum permeability ($1.2566370614. \times 10^{-6}$ $T \cdot m \cdot A^{-1}$)
j Imaginary unit
ω Angular frequency ($rad \cdot Hz$)
t Time (s)
$\boldsymbol{E}$ Electric field ($V \cdot m^{-1}$)
$\boldsymbol{H}$ Magnetic field ($A \cdot m^{-1}$)
P_{PID} PID regulated Cavity length (m)
$e(t)$ Regulated - measured temperature error (K)
K_p PID proportional coefficient
K_I PID integral coefficient
K_DPID derivative coefficient
S_{11} Reflective scattering parameter

1. Introduction

Microwave energy is an efficient way to enable a fast heating of ceramics[1–3]. Unlike resistive processes, a microwaves cavity can be designed to significantly amplify the electric field by resonance and allows the heating of dielectric materials[4] by dielectric dissipation[5]. Numerous studies report a decrease of the sintering temperature by microwave assisted sintering[4,6,7]. The ponderomotive forces is one of the most cited mechanisms for explaining such field effects[8–10]. Nevertheless, the latter phenomenon is not clearly evidenced[11] and other thermal, kinetic mechanisms[12–14] may be present. In the field of 3D printing, debinding and industry, microwave energy has an interest to provide a hybrid heating[1,15–18] reducing the temperature/debinding/sintering differences between the external surfaces and the core of thick specimens (> 5 mm) where crack may appear[19–21]. In the flash sintering domain[22–26], previous cited advantages make microwave energy a very interesting way to provide a fast, volumetric and contactless heating to the specimen. Despite this amazing prospect, there are few studies[27–30] on flash microwave sintering because the following technological issues need to be addressed:

(i) in resistive flash sintering, the whole process can be controlled by a voltage/current control transition making the control of the flash sintering relatively easy because highly sensitive to the electrical current response[22,24,31]. Using microwaves, this way of controlling the flash event cannot be used;

(ii) for microwave sintering, the control needs to be done by non-contact temperature measurement *via* a pyrometer where a PID (proportional integral derivative) regulation drives the flash event avoiding uncontrolled thermal runaway;

(iii) a microwave device requires managing numerous additional parameters closely connected to each other such as the resonance and the efficiency of the heating of the sample affected by the specimen dielectric properties changing with temperature and the frequency variations of the magnetron source;

(iv) the last aspect is the heating stability. In the microwave sintering domain, the direct heating is often very unstable and generates hot spots due to the cooling fluxes at the surfaces and the NTC (negative temperature coefficient) resistivity[18,32,33] of some ceramics like zirconia, silicon carbide, zinc oxide, etc[34]. Susceptors are classically used to follow the heating cycle and balance the thermal field in the specimen[35,36].

The last point is the most important, if the specimen is directly heated, the sintering profile starts from the center and slowly propagates toward the edge[37]. This generally implies cracks in the ceramic if the propagation front is too fast. Most of the time, the propagation front stops as a thermal equilibrium is achieved between the center and the cooler edge. A core shell microstructure distribution is generally observed[29]. In the design of a hybrid heated microwave applicator, the source of cooling fluxes must be identified. In general, the three cooling fluxes are the radiative/convective fluxes toward adjacent refactories insulators and the thermal conduction in the refractory in contact. At high temperature (~1000°C) and for a direct heating configuration, the proportion of each thermal fluxes loss is about 10% conductive, 20% convective and 70% radiative[36]. In function of the configuration, these proportions may evolve depending on the mass of cold refractory in contact, the proportion of air in the cavity (heat losses by convection) and the total area of cold adjacent refractories surfaces, respectively. The multiphysics numerical tool is of great help for assessing these fluxes[17,21,38–40]. If the cooling fluxes are too important, the thermal runaway may not appear[41]. The establishment of a flash sintering configuration should consider the thermal problem and adjusts the critical size of the specimen[42] with the thermal environment[23,43]. This point is discussed in ref[44].

In this context, the present study focuses on the establishment of stable conditions of ultra-rapid microwave sintering of centimetric size zirconia. This study uses a hybrid heating configuration to decrease the specimen cooling fluxes and the thermal gradients *in situ*

generated. Interesting zirconia microstructure/mechanical properties where obtained by microwave sintering [45–47] on few millimeters samples and for typical heating rates of about 50K/min. The purpose of this work is to estimate the sintering speed limit (heating rate limit) of these thick specimen size in terms microstructures, cracks and heating stability. This study includes *in situ* dilatometry to conduct a master sintering curve and investigate the sintering regime of ultra-rapid heating.

2. Experiment and method

2.1. Experimental configuration

The microwave configuration is reported in figure 1. It includes a 2.45GHz microwave generator adapted to an 86×43 mm^2 rectangular waveguide (WR340). This type of waveguide is designed to propagate a 2.45GHz TE_{10} microwave mode. The microwave generator was a 2kW from Sairem (GMP20) coupled with a 2-ports waveguide isolator from Sairem protecting the generator by absorbing the reflected power. This generator part is connected to a resonant cavity made of a 32×36 mm^2 aperture iris and an automated movable short circuit (PCCMOTSBS/EB WR340) from Sairem. In order to ensure a good transmission of the microwaves towards the resonant cavity, a three-stubs impedance tuner (AI3SMWR340 D24×25 from Sairem) is placed between the iris and the isolator. The configuration in the heating zone (applicator) is described in figure 1b, 1c, 1d. Two 20×20×6 mm^3 silicon carbide susceptors are employed to heat in hybrid conditions the zirconia green specimen obtained by cold isostatic pressing (CIP) at 400 MPa. In order to optimize the heating, these susceptors are placed in the electrical field/wave vector plane. In this way, the microwave dissipation is optimal and this configuration is less sensitive to the offsets of the maximum electric field location [48–50]. The pyrometer was placed under the heated sample to provide a measure minimizing the influence of the radiation coming from the susceptor. In addition, this configuration allows measuring the displacement of the specimen during the sintering by a

displacement sensor placed on the top (magnescale DS812SLR purchased from sensel measurements, with measure length 12 mm, resolution 1 µm). An alumina rod is used to penetrate the microwave cavity and transmit the specimen displacement. Each test were duplicated using a fully dense zirconia to retrieve the thermal expansion and calculate the relative density curves. The microstructures have been analyzed *via* SEM on polished surfaces with ZEISS Supra 55 scanning electron microscope (ZEISS, Oberkochen, Germany).

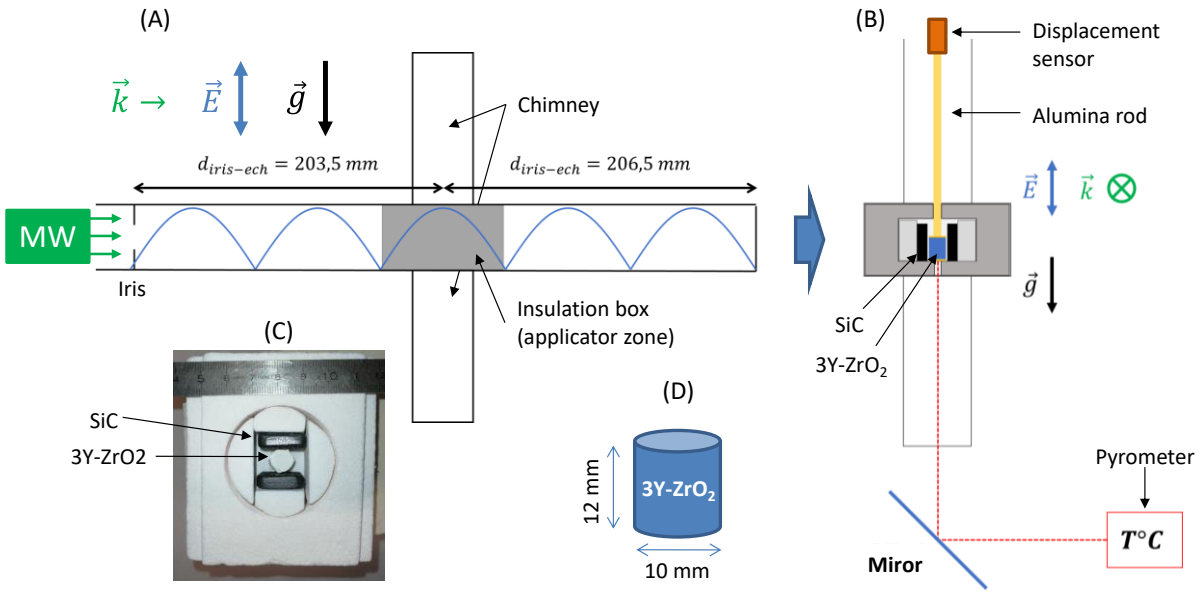

Figure 1 Microwave sintering configuration, (a) applicator geometry, (b) cross-section view, (c) top view photograph, (d) zirconia specimen initial dimensions.

2.2. Method

The objective of this work is to study the ultra-rapid microwave heating and sintering of zirconia in order to determine its feasibility, the sintering kinetics involved and its technological limitations. A zirconia powder (3 mol% Y_2O_3 "TZ-3Y-E", 40nm) was purchased from Tosoh for this study. Similarly to a dilatometry protocol, a first experiment was conducted to record the sintering shrinkage and a second one was done on a fully sintered specimen to subtract the thermal expansion. The relative density curve is then calculated from the corrected sample height curve, the heterogeneity of microwave heating compared to conventional furnace implicates about 2 % of errors in the final relative density curves. The

imposed sintering cycles are reported in figure 2. In the first three minutes, the autoadaptative PID system (proportional integral derivative) applied two thermal pulses at a forward power of 500 W to calculate the PID coefficients. This operation helps ensure a good regulation quality. Nevertheless, as we apply ultra-rapid heating rates (500 K/min), a slowing of the heating rate down to 50 K/min is applied starting from 1450°C. This slowing down is suitable to avoid overshot and it helps stabilize the final stage while continuing the heating for one minute. The obtained dilatometry data were used in a master sintering curve study via a homemade octave-forge script.

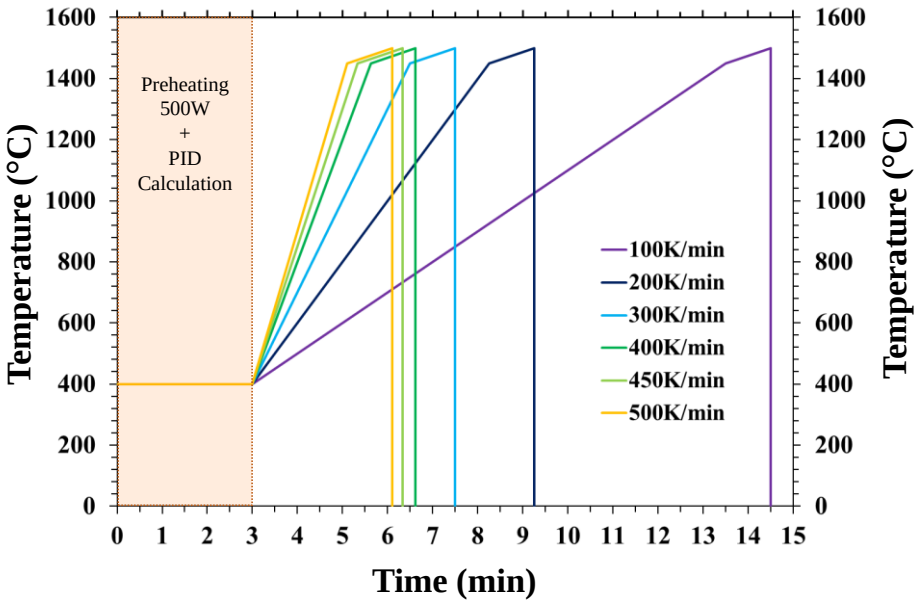

Figure 2 Programmed heating cycles of the study.

In order to complete this experimental study and gain a better understanding of the electromagnetic-thermal behavior of the cavity, a simulation study was conducted with the software COMSOL Multiphysics 5.5. In the following, the model construction and boundary conditions are defined.

3. Theory and calculations

3.1. Microwave heating physics

The simulation work was divided into two parts. In a first stage, a parametric study of a pure electromagnetic problem was solved at room temperature to locate the cavity length at which the resonance is taking place and to plot the internal distribution of the E and H fields. In COMSOL, this problem is solved by Maxwell's equations that can be combined in below equation [17,51]:

$$\nabla \times (\mu_r^{-1} \nabla \times \boldsymbol{E_r}) = k_0^2 \left(\varepsilon_r - \frac{j\sigma}{\omega\, \varepsilon_0}\right) \boldsymbol{E_r} \quad (1)$$

with $\boldsymbol{E_r}$ the harmonic electric field expression $\boldsymbol{E} = \boldsymbol{E_r} exp(j\omega t)$.

Once the resonance cavity length was determined, this length was selected to model the electromagnetic-thermal problem. This fully coupled model calculates the heat transfer (2) based on the volumetric dissipated power (3). In return, the heating part helps actualize the temperature dependent electromagnetic properties of the materials.

$$\rho C_p \frac{\partial T}{\partial t} + \nabla.(-\kappa \nabla T) = Q_e \quad (2)$$

$$Q_e = \frac{\omega}{2}(\varepsilon_0 \varepsilon_r'' \boldsymbol{E}^2 + \mu_0 \mu_r'' \boldsymbol{H}^2) \quad (3)$$

The heat transfer by air convection is modeled through the fluid dynamic equations previously used in [21,36,52]. The temperature dependent electromagnetic properties of the materials can be found in the appendix table of ref[53]. In these data, the effective medium approximation (EMA) was employed to determine the porosity dependence of electromagnetic and thermal conductivity functions. For the density and specific heat product, we have the following relation $\rho C_p = (1-\theta)\rho_{dense} C_{p\,dense}$ for the porous zirconia specimen [54].

3.2. Boundary conditions

A draw of the thermal boundary conditions is reported in figure 3. The external boundary of the insulation box has two surfaces to ambient cooling fluxes conditions (convective and radiative):

$$\varphi_{csa} = h_{ia}(T_{air} - T) \quad (4)$$

$$\varphi_{rsa} = \sigma_s \epsilon ({T_{air}}^4 - T^4) \quad (5).$$

The emissivity ϵ and convection coefficient h_{ia} of 0.8 and 5 $W{\cdot}m^{-2}{\cdot}K^{-1}$, respectively, are defined for the insulation box external surfaces[21]. For the internal solid/air interfaces surface-to-surface thermal radiation is modeled in addition to the natural convection[17]. The relationship between the thermal power radiated $e_b(T)$ and the incoming thermal irradiation G, is defined by the radiosity *J*:

$$J = \rho_r G + \epsilon e_b(T) = \rho_r G + \epsilon n^2 \sigma_s T^4 \quad (6).$$

With the relationship between the emissivity and reflectivity:

$$\epsilon = 1 - \rho_r \quad (7).$$

The expression of the net inward radiative heat flux φ_{rss} is:

$$\varphi_{rss} = \epsilon (G - e_b(T)) \quad (8).$$

The electromagnetic boundary conditions are simple: all internal metallic surfaces are assumed perfectly reflective and a TE_{10} port is inserted at the generator location to simulate both the generator and the isolator. The simulation also includes a numerical PID on the forward microwave power which imposes the thermal cycle to the specimen bottom face (like in the experiment). The PID has the following expression:

$$P_{PID} = K_p e(t) + K_I \int_0^t e(t) d\tau + K_D \frac{de(t)}{dt} \quad (9)$$

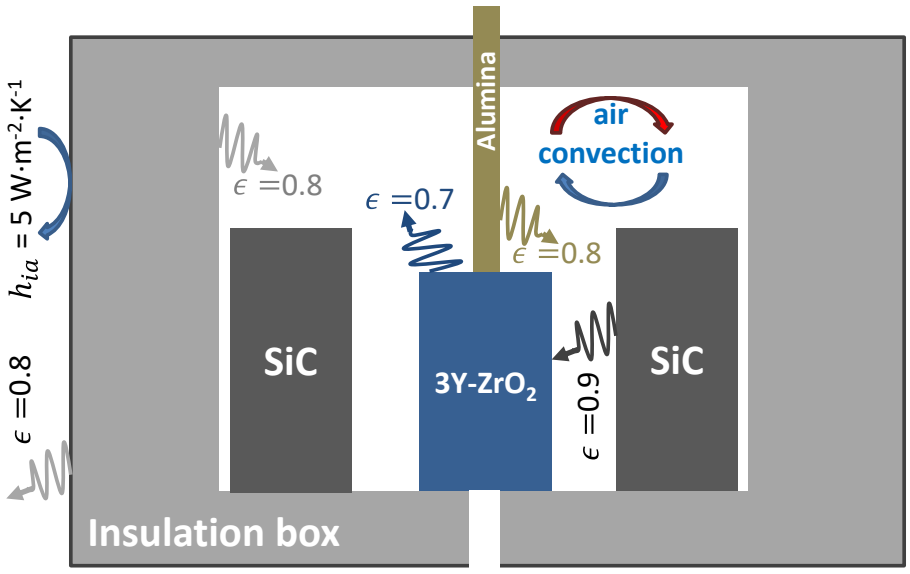

Figure 3 Radiative/convective boundary conditions in the heating zone, the emissivity ϵ values of each material and external conductance h_{ia} are indicated.

4. Results and discussions

4.1. Simulation of the electromagnetic fields

To locate the optimum cavity length from which the resonance phenomenon takes place, the parametric simulation of the cavity has been conducted and is reported in figure 4a. The reflective scattering parameter (S_{11}) indicates the resonance by a minimum value[29]. At 414mm of the cavity length, the S11 parameter is minimal and the electromagnetic fields (reported in figure 4b) are maximum in the cavity. The distribution of the fields indicates a partial shielding of the fields heated region like in [48]. Nevertheless, the electrical field in the zirconia specimen is relatively homogeneous without significant electrical field gradients.

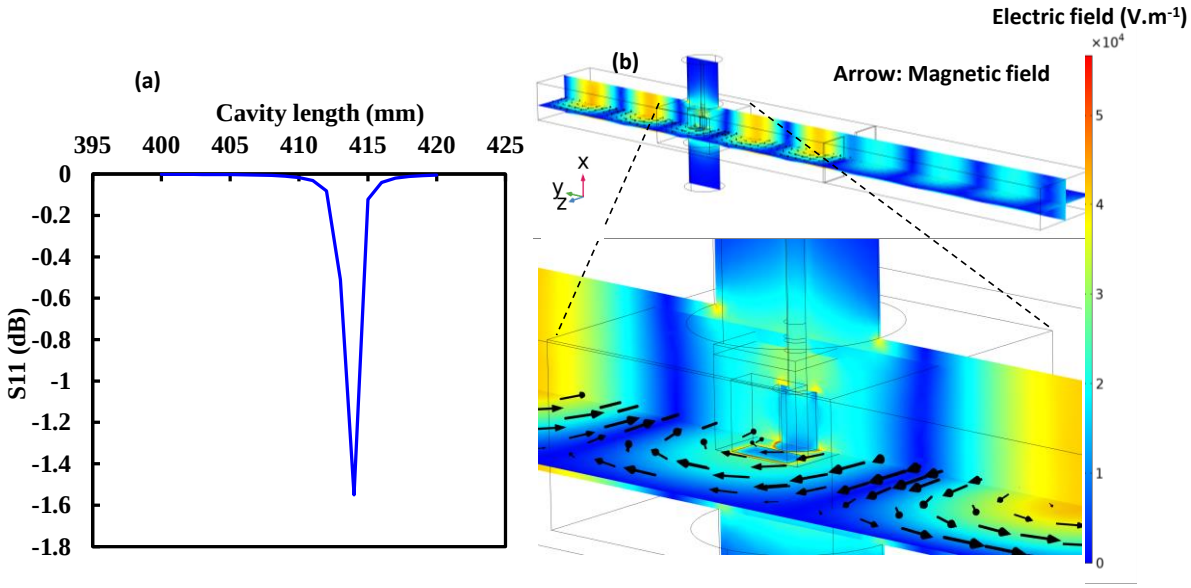

Figure 4 Parametric electromagnetic simulation of the microwave cavity at room temperature, (a) determination of the resonant cavity length, (b) electric/magnetic field distribution at resonance.

4.2. Heating tests

The recorded microwave/thermal data for the experiments 100, 300, 500 K/min are plotted in figure 5. Despite the ultra-rapid heating rates, the regulation follows the set temperature cycle with minimal discrepancies (<1%). The dissipated power is between 200 and 400 W for a transmission of about 65% at high temperature. The cavity and impedance tuner have been fixed to ensure higher heating efficiency at high temperature. The length of the cavity was

maintained constant during the test to avoid multiple parameters changes. Only small impedance adjustments were made during the test if needed.

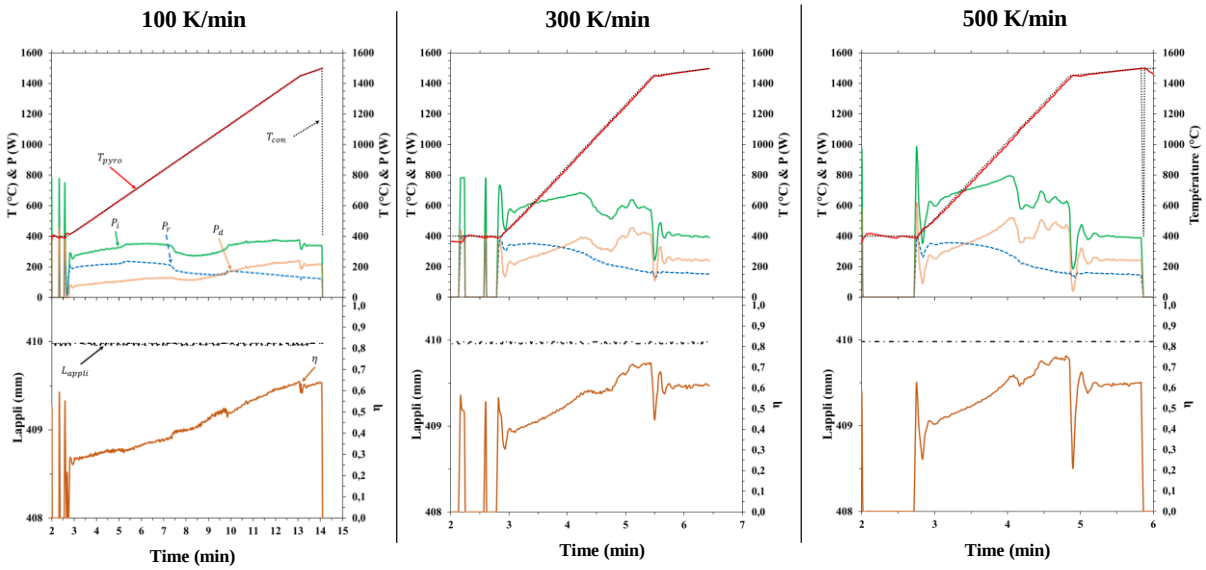

Figure 5 Recorded microwave/thermal data for the experiments at 100, 300, 500 K/min with, the sample temperature (T_{pyro}), set temperature cycle (T_{com}), forward, reflected, dissipated microwave power (P_i, P_r, P_d respectively), return rate (η) and applicator length (Lappli).

If the heating of all samples was successful, a crack appears for the tests at 450 and 500 K/min. This suggests the thermal gradients become too high after 400 K/min and the sintering shrinkage differences cause cracks. Thus, to determine which thermal gradient threshold generates cracks, a simulation of the 400 K/min heating rate is conducted in the following section.

4.3. Electromagnetic-thermal-fluid-dynamic simulation of the heating at 400 K/min

Many physics (electromagnetic waves, heat transfer, air convection and surface to surface radiation) were considered to compute the electromagnetic and temperature fields. The fully coupled electromagnetic-thermal-fluid-dynamic simulation was carried out on half of the cavity to decrease the calculation time to about 2 h. The simulated temperature fields of the 400 K/min heating rate are reported in figure 6a, 6b, 6c. With increasing temperatures, the penetration depth of SiC evolve into millimetric range (near 1200°C [35]) while the zirconia

specimen dielectric behavior evolves from quasi-dielectric behavior at room temperature to semiconducting NTC type after 400°C [17,41]. Consequently, between 400 and 1200°C, a heating regime transition from the SiC heating to zirconia heating is expected. During this transition, the cooling fluxes are expected to increase at the zirconia boundary implying higher temperatures in the center of the sample, leading to thermal gradients at high temperatures. To characterize the temperature evolution in the specimen, 5 temperature probes were virtually introduced at different locations (figure 6d). As observed, SiC susceptors heat preferentially at the beginning of the thermal cycle up to T ≈ 580 °C. Then the heating regime of the overall process switches with a preferential heating of the 3Y-ZrO_2 sample. Thermal gradients appear and increase drastically to a value of 122 K/mm with a final maximum temperature difference of about 730 °C between the middle (T = 1680 °C) and the top of the sample (T = 950 °C) where the cold alumina probe is in contact. This temperature gradient within the sample generates shrinkage differences and a stress that may exceed the resistance of the porous skeleton during sintering. Fully sintered tosoh® zirconia has a bending stress of 1200 MPa[55] but the resistance of the porous skeleton during sintering is much lower than this value[56] and may generate the cracks experimentally observed for higher heating rates.

This high thermal heterogeneity originates from an important cooling by radiation, convection and conduction. To estimate the relative magnitude of those cooling fluxes at the specimen boundaries, the integral of the radiative and convective fluxes in the air/sample interfaces and the integral of the conductive flux (sample/alumina, sample/insulation interfaces) are reported in figure 6e. Using these curves, the ratio of each flux contribution can be determined regarding the process temperature giving the graph presented in figure 6f. It shows a significant drop of the radiative and convective contributions around T ≈ 580°C and demonstrates the switch of the heating regime from SiC susceptors to the 3Y-ZrO_2 sample. This phenomenon is also illustrated by the inversion of the convective velocity field motion during all the process. A video is available in supplementary file. At low temperature, the

convection fluxes follow a circular motion from the SiC, as observed in figure 6g. This phenomenon partially stabilizes the heating and contributes (with surface radiation), to heating of the sample. When zirconia starts to heat preferentially, the radiative flux becomes preeminent until it reaches around 78% of the total thermal flux losses. Then, the circular motion of the convection fluxes originates from the sample and represents 17% of the thermal losses (figure 6f and g). Finally, at high temperature, the conductive part, located at the sample/insulation and the sample/alumina rod boundaries, represents only 5 %, which is consistent with the proportion of thermal fluxes loss for a direct heating configuration [36].

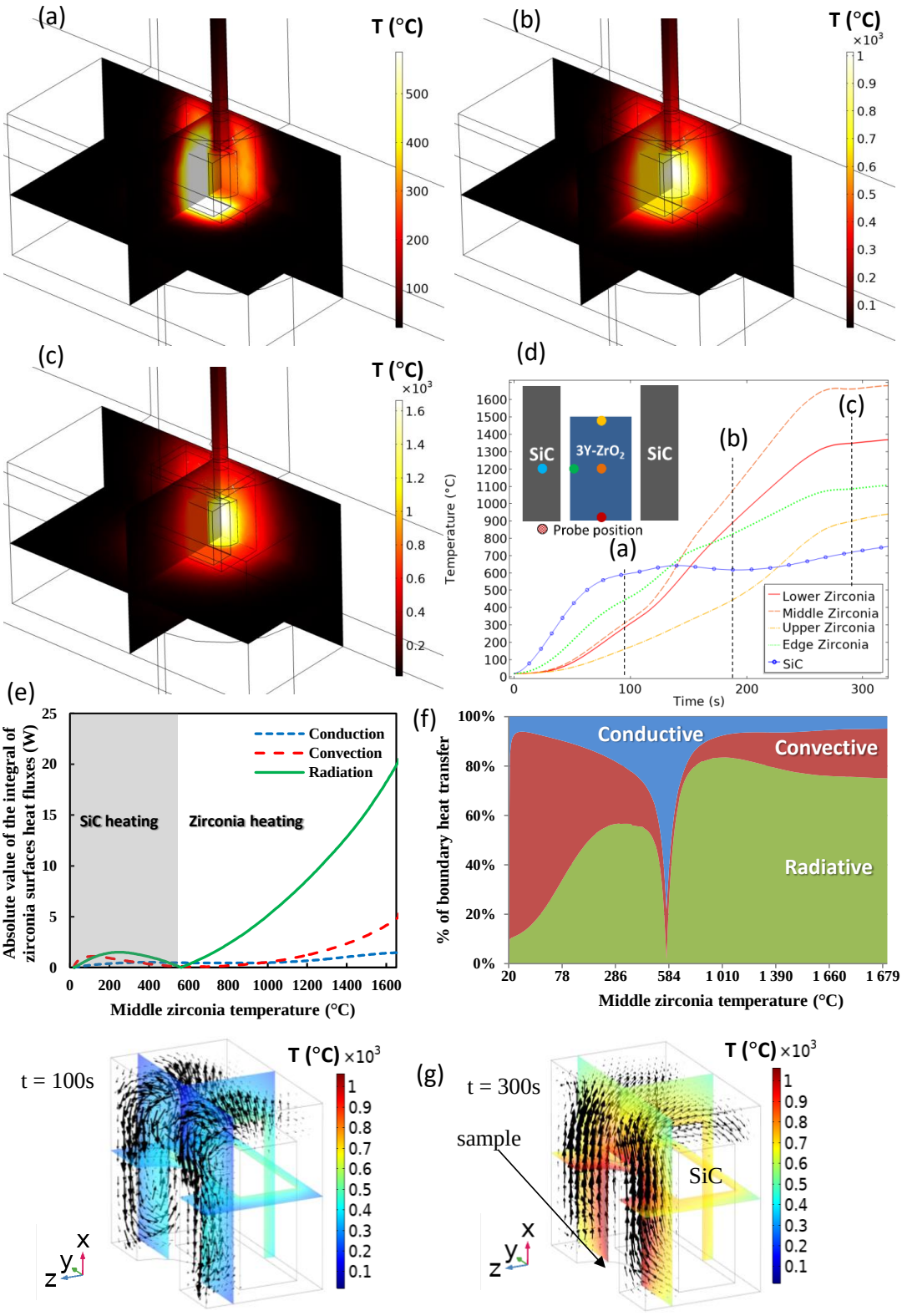

Figure 6 Electromagnetic-thermal-fluid-dynamic simulation of the 400 K/min test, simulated thermal field at (a) t=90 s (b) t= 180s and (c)=280s, (d) temperature evolution during microwave heating, the PID was based on the average bottom specimen surface temperature, (e) integral of the cooling fluxes through zirconia specimen surfaces and corresponding cooling fluxes ratio diagram (f), simulated air convection relative velocity and temperature at t=100s and 300s (g).

4.4. Dilatometry and sintering kinetics analysis

The relative density curves are reported in figure 7. The first graph on the left shows the evolution of the relative density as a function of time, the sintering times evolve from 6 minutes for 100 K/min to value close to 1 min for 400 K/min. A high hybrid heating rate allows to significantly decrease the sintering time to values approaching flash sintering (< 60 sec). In the graph on the right, we can see the sintering temperatures range is 1000-1500°C with about 1250°C of sintering inflection point. It is interesting to compare this with conventional sintering of the same powder [57] at 3, 6, 10 K/min where the sintering temperature are between 1000 and 1300°C. The microwave sintering temperatures are similar to those of conventional sintering while lower sintering values are often observed in microwave sintering [4,6,7]. However, it should be cautiously interpreted as an underestimation of the temperature can be made (see the temperature differences simulated in the specimen itself in figure 6). The important coupling of zirconia at high temperature tends to generate higher temperatures in the center and sometime hot spots [17,41], which generate cracks like those occurring on materials subjected to heating rates higher than 400 K/min.

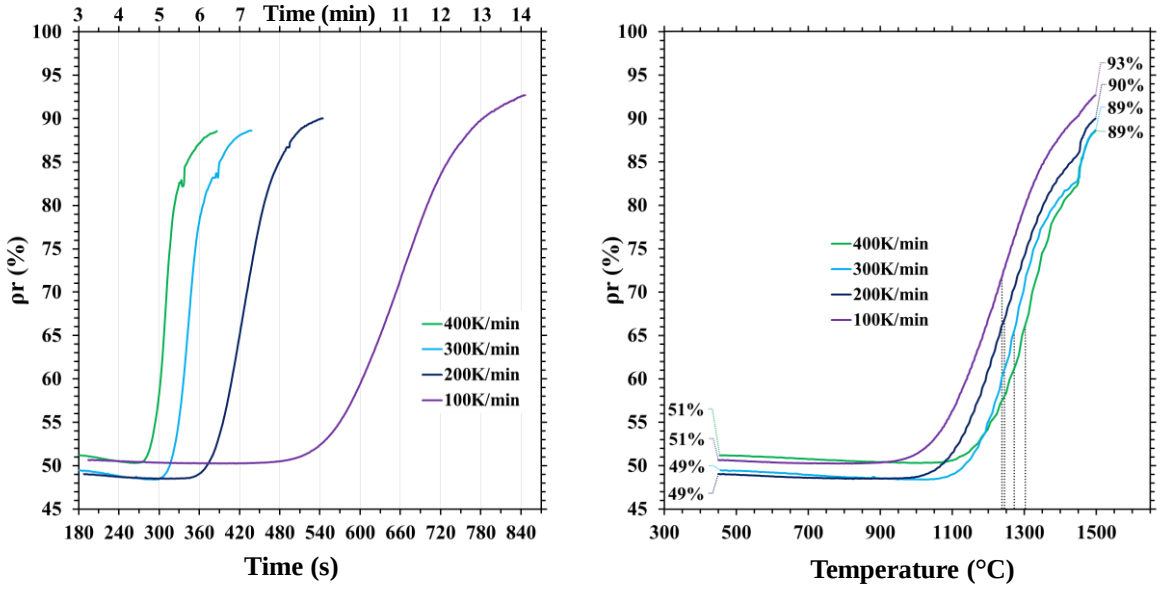

Figure 7 Relative density curves calculated from the displacement sensor and retrieving the thermal expansion by separates tests on fully dense zirconia for the 100, 200,300, 400 K/min tests (the black dashed line indicates the sintering curves inflection point which is about 1250°C).

Nevertheless, obtaining an estimation of the temperature in the core and at the edge of the sample is very challenging and a microwave or kinetic effects cannot be excluded. To go further with this ultra-rapid microwave dilatometry data, a master sintering curve is conducted with the tests at 100, 200, 400 K/min. The results are reported in figure 8. We obtained an activation energy of 225 kJ/mol which is significantly lower than the 625 kJ/mol obtained by conventional sintering at the heating rates of 3, 6, 10 K/min [57]. The specimen temperature gradients may disturb the sintering kinetics on such a big specimen for high heating rates. Beside the latter issues which are still difficult to address experimentally, this result suggests that the ultra-rapid microwave sintering has a very different sintering regime compared to conventional sintering. Numerous phenomena may explain this different behavior, such as the ponderomotive forces, a difference on driving force, concentration of defects, by resulting from the fields and also kinetics effects such as a delay in the pore surface diffusion due to the high heating rates[2,8,9,12,14,58].

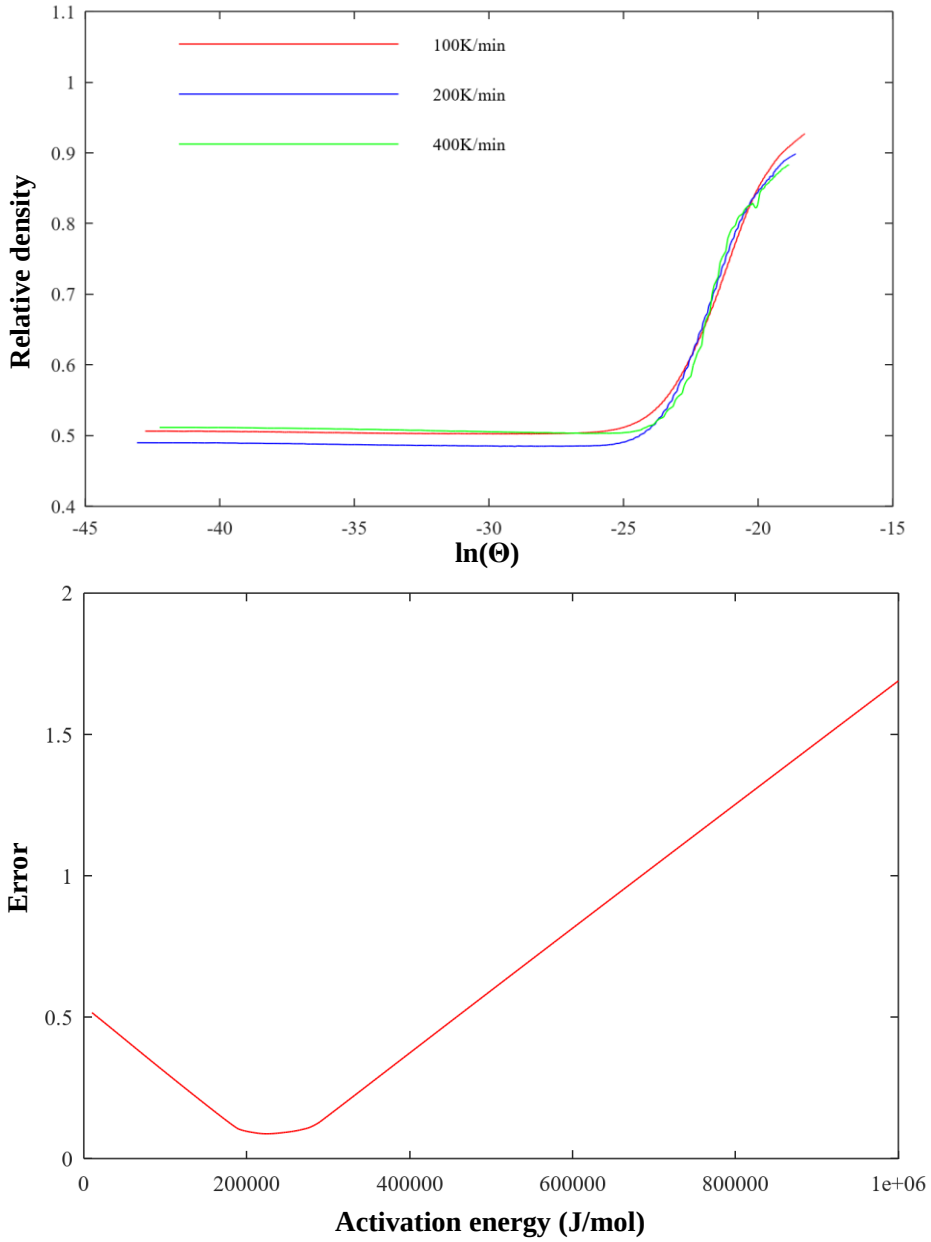

Figure 8 Master sintering curve study of the 100, 200 and 400 K/min tests.

4.5. Microstructures

The SEM images of the sintered specimens are reported in figure 9. All of them show submicronic microstructures with similar grains size close to 350 nm. A high level of porosity (about 10 %) is observed in accordance with the dilatometry curves in figure 7. Compared to conventional sintering, the ultra-rapid sintering seems to favor the fast sintering of highly agglomerated zones (like reported for TEM images of the powder[59]) generating bigger surrounding pores (see figure 9). For the test at 100 and 400 K/min, it is interesting to see the shape of the internal pore triple point. The later exhibits a very sharp shape suggesting a significant delay of the pore coarsening by surface diffusion. In conventional sintering, the long sintering time typically allowing the pore surface diffusion to quickly stabilize the pore surfaces that become nearly spherical.

The presence of large size porosity for increasing heating rates is observed. This may be due to different potential hypothesis like a boating effect of residual organic/carbon pollution as fully densified zones are also present. In principle, this powder is binderless. However, trace of binder, dispersant or plasticizer may still be present. Another explanation can be the difference of the core/edge sintering speed due to the thermal gradient (see simulation figure 6) that may favor coarsening rather than sintering.

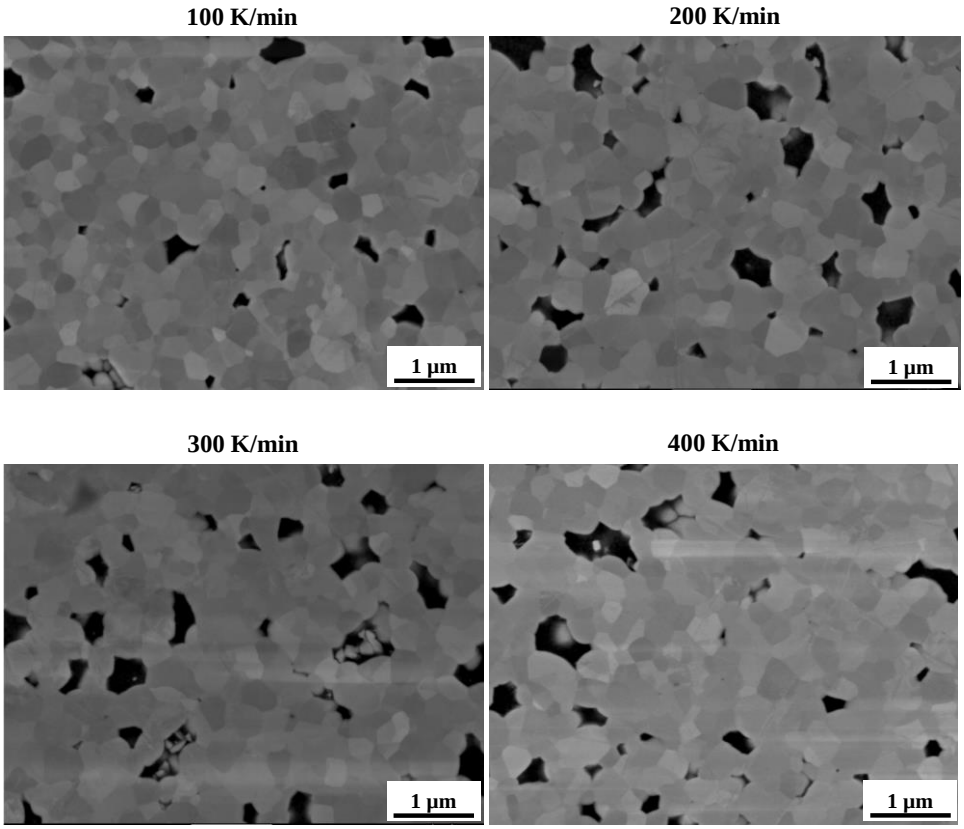

Figure 9 SEM images of the sintered samples at 100, 200, 300, and 400 K/min

5. Conclusion

In this work, the microwave sintering of zirconia from typical (100 K. min^{-1}) to ultra-rapid (500 $K.min^{-1}$) heating rates has been studied, using typical hybrid heating configuration.

The sintering of zirconia was successful until 400 $K.min^{-1}$, allowing sintering time values close of about 60s. High remaining porosity is still present possibly due to the thermal gradients or remaining carbon pollution. Based on dilatometry measurements, a master sintering curve has been conducted. Both ultra-rapid microwave and conventional sintering have been compared. With respectively 225 $kJ.mol^{-1}$ and 625 $kJ.mol^{-1}$, the low activation energy obtained for the ultra-rapid microwave sintering suggests a different sintering regime due to the high heating rates, but precautions must be taken for the interpretation as temperature measurement is always an uneasy task during microwave sintering.

The fully coupled electromagnetic-thermal-fluid-dynamic simulation at 400 $K.min^{-1}$ demonstrated important thermal gradients. A difference of 570°C has been therefore

simulated between the core and the top of the sample, where the cold alumina probe is in contact. This temperature difference undoubtedly led to shrinkage differences during the sintering, responsible for the cracks experimentally observed for the higher heating rates. The contribution of the conductive, convective and radiative cooling fluxes has been also studied during all the process. The switch of the heating regime, from SiC susceptors to the 3Y-ZrO_2 sample around T = 580°C (obtained from modeling), comes with a significant drop of the radiative exchange and the inversion of the convective motion. At high temperature, the quantification of each cooling flux gives 78% radiative, 17% convective, 5% conductive. This numerical tool will allow improving the design of the hybrid configuration to reduce cooling effects and achieve optimal conditions for fast microwave sintering.

Supplementary material

S1 Video of the 500K/min test simulated air temperature and convection motion.

Acknowledgements

This study was funded by the French National Research Agency (ANR), project ULTRARAPIDE N°ANR-19-CE08-0033-01.

The help and support of Christophe Couder, Jérôme Lecourt and Christelle Bilot is gratefully acknowledged.

Data availability

The raw/processed data required to reproduce these findings cannot be shared at this time due to technical or time limitations.

Credit authorship contribution statement

Charles Manière: Conceptualization, Supervision, Modeling, Writing, **Christelle Harnois:** Conceptualization, Supervision, review & editing; **Guillaume Riquet**: Modeling;

Thomas Grippi: Calculations; **Stéphanie Behar-Lafenetre:** review & editing; **Sylvain Marinel:** Conceptualization, Supervision, review & editing;.

References

1. Rybakov KI, Olevsky EA, Krikun E V. Microwave Sintering: Fundamentals and Modeling. Green DJ, editor. J Am Ceram Soc [Internet]. 2013 Apr;96(4):1003–20. Available from: http://doi.wiley.com/10.1111/jace.12278
2. Olevsky EA, Dudina D V. Field-Assisted Sintering [Internet]. Springer N. Cham: Springer International Publishing; 2018. 425 p. Available from: http://link.springer.com/10.1007/978-3-319-76032-2
3. Bordia RK, Kang S-JL, Olevsky EA. Current understanding and future research directions at the onset of the next century of sintering science and technology. J Am Ceram Soc [Internet]. 2017 Jun;100(6):2314–52. Available from: http://doi.wiley.com/10.1111/jace.14919
4. Croquesel J, Bouvard D, Chaix J-M, Carry CP, Saunier S. Development of an instrumented and automated single mode cavity for ceramic microwave sintering: Application to an alpha pure alumina powder. Mater Des [Internet]. 2015 Dec;88:98–105. Available from: http://linkinghub.elsevier.com/retrieve/pii/S0264127515303713
5. Sun J, Wang W, Yue Q. Review on Microwave-Matter Interaction Fundamentals and Efficient Microwave-Associated Heating Strategies. Materials (Basel) [Internet]. 2016 Mar 25;9(4):231. Available from: http://www.mdpi.com/1996-1944/9/4/231
6. Zuo F, Saunier S, Meunier C, Goeuriot D. Non-thermal effect on densification kinetics during microwave sintering of α-alumina. Scr Mater [Internet]. 2013 Aug;69(4):331–3. Available from: http://linkinghub.elsevier.com/retrieve/pii/S1359646213002649
7. Wroe R, Rowley AT. Evidence for a non-thermal microwave effect in the sintering of partially stabilized zirconia. J Mater Sci [Internet]. 1996;31(8):2019–26. Available from: http://link.springer.com/10.1007/BF00356621
8. Rybakov KI, Olevsky EA, Semenov VE. The microwave ponderomotive effect on ceramic sintering. Scr Mater [Internet]. 2012 Jun;66(12):1049–52. Available from: http://linkinghub.elsevier.com/retrieve/pii/S1359646212001571
9. Olevsky EA, Maximenko AL, Grigoryev EG. Ponderomotive effects during contact formation in microwave sintering. Model Simul Mater Sci Eng [Internet]. 2013 Jul 1;21(5):055022. Available from: http://stacks.iop.org/0965-0393/21/i=5/a=055022?key=crossref.95642f4fe0bbf9bee0527ed1bcfc877e
10. Raj R, Cologna M, Francis JSC. Influence of Externally Imposed and Internally Generated Electrical Fields on Grain Growth, Diffusional Creep, Sintering and Related Phenomena in Ceramics. Green DJ, editor. J Am Ceram Soc [Internet]. 2011 Jul;94(7):1941–65. Available from: http://doi.wiley.com/10.1111/j.1551-2916.2011.04652.x
11. Macaigne R, Marinel S, Goeuriot D, Saunier S. Sintering paths and mechanisms of pure MgAl2O4 conventionally and microwave sintered. Ceram Int [Internet]. 2018 Dec;44(17):21107–13. Available from: https://linkinghub.elsevier.com/retrieve/pii/S0272884218322120
12. Olevsky EA, Kandukuri S, Froyen L. Consolidation enhancement in spark-plasma sintering: Impact of high heating rates. J Appl Phys [Internet]. 2007 Dec;102(11):114913. Available from: http://aip.scitation.org/doi/10.1063/1.2822189
13. Hansen JD, Rusin RP, Teng M-H, Johnson DL. Combined-Stage Sintering Model. J Am Ceram Soc [Internet]. 1992 May;75(5):1129–35. Available from: http://doi.wiley.com/10.1111/j.1151-2916.1992.tb05549.x

14. Ji W, Parker B, Falco S, Zhang JY, Fu ZY, Todd RI. Ultra-fast firing: Effect of heating rate on sintering of 3YSZ, with and without an electric field. J Eur Ceram Soc [Internet]. 2017 Jun;37(6):2547–51. Available from: http://linkinghub.elsevier.com/retrieve/pii/S0955221917300481
15. Oghbaei M, Mirzaee O. Microwave versus conventional sintering: A review of fundamentals, advantages and applications. J Alloys Compd [Internet]. 2010 Apr;494(1–2):175–89. Available from: http://linkinghub.elsevier.com/retrieve/pii/S0925838810001015
16. Croquesel J, Bouvard D, Chaix J-M, Carry CP, Saunier S, Marinel S. Direct microwave sintering of pure alumina in a single mode cavity: Grain size and phase transformation effects. Acta Mater [Internet]. 2016 Sep;116:53–62. Available from: https://linkinghub.elsevier.com/retrieve/pii/S1359645416304463
17. Manière C, Zahrah T, Olevsky EA. Fully coupled electromagnetic-thermal-mechanical comparative simulation of direct vs hybrid microwave sintering of 3Y-ZrO2. J Am Ceram Soc [Internet]. 2017 Mar;100(6):2439–2450. Available from: http://doi.wiley.com/10.1111/jace.14762
18. Yakovlev V V, Allan SM, Fall ML, Shulman HS. Computational Study of Microwave Processing of thermal runaway in microwave processing Zirconia. In: Tao JCE, editor. Microwave and RF Power Applications [Internet]. Toulouse; 2011. p. 303–6. Available from: https://users.wpi.edu/~vadim/AMPERE-2011-125.pdf
19. Bae C-J, Halloran JW. Influence of Residual Monomer on Cracking in Ceramics Fabricated by Stereolithography. Int J Appl Ceram Technol [Internet]. 2011 Nov;8(6):1289–95. Available from: http://doi.wiley.com/10.1111/j.1744-7402.2010.02578.x
20. Li H, Song L, Sun J, Ma J, Shen Z. Dental ceramic prostheses by stereolithography-based additive manufacturing: potentials and challenges. Adv Appl Ceram [Internet]. 2019 Feb 17;118(1–2):30–6. Available from: https://www.tandfonline.com/doi/full/10.1080/17436753.2018.1447834
21. Manière C, Zahrah T, Olevsky EA. Fluid dynamics thermo-mechanical simulation of sintering: Uniformity of temperature and density distributions. Appl Therm Eng [Internet]. 2017 Aug;123:603–13. Available from: http://linkinghub.elsevier.com/retrieve/pii/S1359431117322032
22. Cologna M, Rashkova B, Raj R. Flash Sintering of Nanograin Zirconia in <5 s at 850°C. J Am Ceram Soc [Internet]. 2010 Nov;93(11):3556–9. Available from: http://doi.wiley.com/10.1111/j.1551-2916.2010.04089.x
23. Biesuz M, Sglavo VM. Flash sintering of ceramics. J Eur Ceram Soc. 2019 Feb;39(2–3):115–43.
24. Dancer CEJ. Flash sintering of ceramic materials. Mater Res Express [Internet]. 2016 Oct 10;3(10):102001. Available from: http://stacks.iop.org/2053-1591/3/i=10/a=102001?key=crossref.927435991fe887d465218f659badc084
25. Yu M, Grasso S, Mckinnon R, Saunders T, Reece MJ. Review of flash sintering: materials, mechanisms and modelling. Adv Appl Ceram [Internet]. 2017 Jan 2;116(1):24–60. Available from: https://www.tandfonline.com/doi/full/10.1080/17436753.2016.1251051
26. Luo J. The scientific questions and technological opportunities of flash sintering: From a case study of ZnO to other ceramics. Scr Mater [Internet]. 2018 Mar;146:260–6. Available from: https://linkinghub.elsevier.com/retrieve/pii/S1359646217307066
27. Bykov Y V., Egorov S V., Eremeev AG, Kholoptsev V V., Rybakov KI, Sorokin AA. Flash Microwave Sintering of Transparent Yb:(LaY) 2 O 3 Ceramics. Olevsky E, editor. J Am Ceram Soc [Internet]. 2015 Nov;98(11):3518–24. Available from: http://doi.wiley.com/10.1111/jace.13809
28. Bykov Y, Egorov S, Eremeev A, Kholoptsev V, Plotnikov I, Rybakov K, et al. On the Mechanism of Microwave Flash Sintering of Ceramics. Materials (Basel) [Internet].

2016 Aug 11;9(8):684. Available from: http://www.mdpi.com/1996-1944/9/8/684
29. Manière C, Lee G, Torresani E, Gerling JF, Yakovlev V V., Martin D, et al. Flash microwave pressing of zirconia. J Am Ceram Soc [Internet]. 2020 Aug 19;103(8):4110–21. Available from: https://onlinelibrary.wiley.com/doi/abs/10.1111/jace.17072
30. Bykov Y V., Egorov S V., Eremeev AG, Plotnikov I V., Rybakov KI, Sorokin AA, et al. Flash Sintering of Oxide Ceramics under Microwave Heating. Tech Phys [Internet]. 2018 Mar 4;63(3):391–7. Available from: http://link.springer.com/10.1134/S1063784218030052
31. Biesuz M, Sglavo VM. Flash sintering of ceramics. J Eur Ceram Soc [Internet]. 2019 Feb;39(2–3):115–43. Available from: https://linkinghub.elsevier.com/retrieve/pii/S0955221918305442
32. Gaone JM, Tilley BS, Yakovlev V V. Electromagnetic heating control via high-frequencyresonance of a triple-layer laminate. J Eng Math [Internet]. 2019 Feb 4;114(1):65–86. Available from: http://link.springer.com/10.1007/s10665-018-9982-6
33. Mohekar A, Tilley B, Yakovlev V. Plane wave irradiation of a layered system: resonance-based control over thermal runaway. In: Proceedings 17th International Conference on Microwave and High Frequency Heating [Internet]. Valencia: Universitat Politècnica de València; 2019. p. 292–311. Available from: http://ocs.editorial.upv.es/index.php/AMPERE2019/AMPERE2019/paper/view/9940
34. Garnault T, Bouvard D, Chaix J-M, Marinel S, Harnois C. Is direct microwave heating well suited for sintering ceramics? Ceram Int [Internet]. 2021 Jun;47(12):16716–29. Available from: https://linkinghub.elsevier.com/retrieve/pii/S0272884221006210
35. Heuguet R, Marinel S, Thuault A, Badev A. Effects of the Susceptor Dielectric Properties on the Microwave Sintering of Alumina. Reimanis I, editor. J Am Ceram Soc [Internet]. 2013 Dec;96(12):3728–36. Available from: http://doi.wiley.com/10.1111/jace.12623
36. Manière C, Borie F, Marinel S. Impact of convection and radiation on direct/hybrid heating stability of field assisted sintering. J Manuf Process [Internet]. 2020 Aug;56:147–57. Available from: https://linkinghub.elsevier.com/retrieve/pii/S1526612520302978
37. Rybakov KI, Egorov S V., Eremeev AG, Kholoptsev V V., Plotnikov I V., Sorokin AA. Ultra-rapid microwave sintering employing thermal instability and resonant absorption. J Mater Res [Internet]. 2019 Aug 14;34(15):2620–34. Available from: http://link.springer.com/10.1557/jmr.2019.232
38. Hachem E, Digonnet H, Massoni E, Coupez T. Immersed volume method for solving natural convection, conduction and radiation of a hat-shaped disk inside a 3D enclosure. Int J Numer Methods Heat Fluid Flow [Internet]. 2012 Aug 3;22(6):718–41. Available from: http://www.emeraldinsight.com/doi/10.1108/09615531211244871
39. Grasso S, Sakka Y, Rendtorff N, Hu C, Maizza G, Borodianska H, et al. Modeling of the temperature distribution of flash sintered zirconia. J Ceram Soc Japan [Internet]. 2011;119(1386):144–6. Available from: http://joi.jlc.jst.go.jp/JST.JSTAGE/jcersj2/119.144?from=CrossRef
40. Hewitt IJ, Lacey AA, Todd RI. A Mathematical Model for Flash Sintering. Alfaro M, Apreutesei N, Davidson F, Volpert V, editors. Math Model Nat Phenom [Internet]. 2015 Oct 2;10(6):77–89. Available from: http://www.mmnp-journal.org/10.1051/mmnp/201510607
41. Manière C, Zahrah T, Olevsky EA. Inherent heating instability of direct microwave sintering process: Sample analysis for porous 3Y-ZrO2. Scr Mater [Internet]. 2017 Feb;128:49–52. Available from: http://linkinghub.elsevier.com/retrieve/pii/S1359646216305036
42. Dong Y. On the Hotspot Problem in Flash Sintering. arXiv [Internet]. 2017;1702.05565. Available from: https://arxiv.org/abs/1702.05565

43. Biesuz M, Dong J, Fu S, Liu Y, Zhang H, Zhu D, et al. Thermally-insulated flash sintering. Scr Mater [Internet]. 2019 Mar;162:99–102. Available from: https://linkinghub.elsevier.com/retrieve/pii/S1359646218306717
44. Jones GM, Biesuz M, Ji W, John SF, Grimley C, Manière C, et al. Promoting microstructural homogeneity during flash sintering of ceramics through thermal management. MRS Bull [Internet]. 2021 Jan 18;46(1):59–66. Available from: https://link.springer.com/10.1557/s43577-020-00010-2
45. Wilson J, Kunz SM. Microwave Sintering of Partially Stabilized Zirconia. J Am Ceram Soc [Internet]. 1988 Jan;71(1):C-40-C–41. Available from: https://onlinelibrary.wiley.com/doi/10.1111/j.1151-2916.1988.tb05778.x
46. Nightingale SA, Dunne DP, Worner HK. Sintering and grain growth of 3 mol% yttria zirconia in a microwave field. J Mater Sci [Internet]. 1996 Oct 1;31(19):5039–43. Available from: http://link.springer.com/10.1007/BF00355903
47. Upadhyaya DD, Ghosh A, Dey GK, Prasad R, Suri AK. Microwave sintering of zirconia ceramics. J Mater Sci [Internet]. 2001;36(October 2001):4707–4710. Available from: https://doi.org/10.1023/A:1017966703650
48. Marinel S, Manière C, Bilot A, Bilot C, Harnois C, Riquet G, et al. Microwave Sintering of Alumina at 915 MHz: Modeling, Process Control, and Microstructure Distribution. Materials (Basel) [Internet]. 2019 Aug 9;12(16):2544. Available from: https://www.mdpi.com/1996-1944/12/16/2544
49. Marinel S, Renaut N, Savary E, Macaigne R, Riquet G, Coureau C, et al. Tuning, Impedance Matching, and Temperature Regulation during High-Temperature Microwave Sintering of Ceramics. Adv Mater Sci Eng [Internet]. 2018;2018:1–8. Available from: https://www.hindawi.com/journals/amse/2018/4158969/
50. Ghorbel I, Ganster P, Moulin N, Meunier C, Bruchon J. Experimental and numerical thermal analysis for direct microwave heating of silicon carbide. J Am Ceram Soc [Internet]. 2021 Jan 14;104(1):302–12. Available from: https://onlinelibrary.wiley.com/doi/10.1111/jace.17451
51. Otin R. Regularized Maxwell Equations and Nodal Finite Elements for Electromagnetic Field Computations. Electromagnetics [Internet]. 2010 Mar 9;30(1–2):190–204. Available from: http://www.tandfonline.com/doi/abs/10.1080/02726340903485489
52. Egorov S V., Rybakov KI, Semenov VE, Bykov Y V., Kanygina ON, Kulumbaev EB, et al. Role of convective heat removal and electromagnetic field structure in the microwave heating of materials. J Mater Sci [Internet]. 2007 Mar 7;42(6):2097–104. Available from: http://link.springer.com/10.1007/s10853-006-0157-x
53. Manière C, Lee G, Zahrah T, Olevsky EA. Microwave flash sintering of metal powders: From experimental evidence to multiphysics simulation. Acta Mater [Internet]. 2018 Apr;147:24–34. Available from: http://linkinghub.elsevier.com/retrieve/pii/S135964541830048X
54. Goto S, Matsubayashi O. Relations between the thermal properties and porosity of sediments in the eastern flank of the Juan de Fuca Ridge. Earth, Planets Sp [Internet]. 2009 Jul 31;61(7):863–70. Available from: https://earth-planets-space.springeropen.com/articles/10.1186/BF03353197
55. Tosoh. Web page [Internet]. 2020. Available from: https://www.tosoh.com/our-products/advanced-materials/zirconia-powders
56. Ryshkewitch E. Compression Strength of Porous Sintered Alumina and Zirconia. J Am Ceram Soc [Internet]. 1953 Feb;36(2):65–8. Available from: https://onlinelibrary.wiley.com/doi/10.1111/j.1151-2916.1953.tb12837.x
57. Manière C, Grippi T, Marinel S. Estimate microstructure development fromsintering shrinkage: a kinetic field approach. Mater Today Commun. 2022;
58. Holland TB, Anselmi-Tamburini U, Quach D V., Tran TB, Mukherjee AK. Effects of local Joule heating during the field assisted sintering of ionic ceramics. J Eur Ceram

Soc [Internet]. 2012 Nov;32(14):3667–74. Available from: http://linkinghub.elsevier.com/retrieve/pii/S0955221912001070
59. Majidi H, Holland TB, van Benthem K. Quantitative analysis for in situ sintering of 3% yttria-stablized zirconia in the transmission electron microscope. Ultramicroscopy [Internet]. 2015 May;152:35–43. Available from: https://linkinghub.elsevier.com/retrieve/pii/S030439911400268X

Figure captions

Figure 1 Microwave sintering configuration, (a) applicator geometry, (b) cross-section view, (c) top view photograph, (d) zirconia specimen initial dimensions.

Figure 2 Programmed heating cycles of the study.

Figure 3 Radiative/convective boundary conditions in the heating zone, the emissivity ϵ values of each material and external conductance h_{ia} are indicated.

Figure 4 Parametric electromagnetic simulation of the microwave cavity at room temperature, (a) determination of the resonant cavity length, (b) electric/magnetic field distribution at resonance.

Figure 5 Recorded microwave/thermal data for the experiments at 100, 300, 500 K/min with, the sample temperature (T_{pyro}), set temperature cycle (T_{com}), forward, reflected, dissipated microwave power (P_i, P_r, P_d respectively), return rate (η) and applicator length (Lappli).

Figure 6 Electromagnetic-thermal-fluid-dynamic simulation of the 400 K/min test, simulated thermal field at (a) t=90 s (b) t= 180s and (c)=280s, (d) temperature evolution during microwave heating, the PID was based on the average bottom specimen surface temperature, (e) integral of the cooling fluxes through zirconia specimen surfaces and corresponding cooling fluxes ratio diagram (f), simulated air convection relative velocity and temperature at t=100s and 300s (g).

Figure 7 Relative density curves calculated from the displacement sensor and retrieving the thermal expansion by separates tests on fully dense zirconia for the 100, 200,300, 400 K/min tests (the black dashed line indicates the sintering curves inflection point which is about 1250°C).

Figure 8 Master sintering curve study of the 100, 200 and 400 K/min tests.

Figure 9 SEM images of the sintered samples at 100, 200, 300, and 400 K/min